Article

Electrolyte design for lithium-ion batteries with a cobalt-free cathode and silicon oxide anode

Seongjae Ko [1], Xiao Han[1], Tatau Shimada[1], Norio Takenaka [1], Yuki Yamada [1] & Atsuo Yamada [1,2] ✉

Lithium-ion batteries (LIBs) to power electric vehicles play an increasingly important role in the transition to a carbon neutral transportation system. However, at present the chemistry of LIBs requires, among other elements, cobalt (Co), which will probably become scarce over time in addition to posing supply chain risks related to its single source, human rights and mining practices. To address this problem, we construct a LIB pairing a Co-free cathode with a silicon suboxide (SiO_x) anode that possesses a high cut-off voltage of 4.9 V and sustains unprecedented 1,000 cycles. Underlying this favourable electrode combination is a rational electrolyte design based on 3.4 M LiFSI/FEMC featuring a shifted potential, which serves to aid formation of robust passivation layers on the anode and promote electrolyte stability against both reductive and oxidative degradations. Our electrolyte formulation offers a pathway towards both sustainable and high-performing LIBs, while the concept could be applied to other electrochemical energy technologies.

Lithium-ion batteries (LIBs) play an essential role in enabling the transition to a sustainable society with reduced carbon emissions by supporting clean energy generation, green transportation and more efficient energy use. It is widely expected that achieving a lower carbon and greener future will rely on the development of LIBs with high energy density (high capacity and high voltage), high environmental friendliness and low cost (Earth abundance).

The chemistry of LIBs, with carbon-based negative electrodes (anodes) and metal oxide-based positive electrodes (cathodes), has remained largely unchanged since their commercialization in 1991 by Sony and Asahi Kasei. In particular, Co has been widely employed in cathode materials because it provides a reasonable reaction potential (Co^{4+}/Co^{3+}; ≥3.8 V versus Li/Li⁺) and improves the electronic/ionic conductivity and structural integrity of cathodes[1,2]. For example, layered oxides $LiCoO_2$, $LiNi_xCo_yMn_zO_2$ and $LiNi_xCo_yAl_zO_2$ provide high practical capacities (~220 mAh g⁻¹), high rate capabilities and extended cycle life, and, thus, are utilized in diverse batteries for use in mobile phones,

electric vehicles and large-scale energy storage systems. However, Co is mined as a by-product of Ni and Cu ores in specific areas (Democratic Republic of Congo), thus raising concerns of an economically and geopolitically constrained supply chain[3–5]. The problem of child labour in the mining of this toxic mineral is also a severe ethical and health concern[3].

In this regard, considerable efforts have been focused on eliminating Co from cathodes. Among the various Co-free materials developed over the past decades, spinel $LiNi_{0.5}Mn_{1.5}O_4$ is one of the favourite candidates due to its high operating potential (average 4.7 V versus Li/Li⁺)[5]. However, its theoretical capacity (C_T, 147 mAh g⁻¹) is lower than that of Co-based layered oxides currently in use[5]. To meet the growing demand for high-energy-density batteries, the replacement of a carbon anode (graphite; C_T = 372 mAh g⁻¹ at ≤0.1 V versus Li/Li⁺) with a high-capacity and Earth-abundant silicon suboxide (SiO_x) anode (C_T = 1,965–4,200 mAh g⁻¹ with 2 ≥ x ≥ 0 at ≤0.4 V versus Li/Li⁺) should also be considered concurrently. This ideal SiO_x|$LiNi_{0.5}Mn_{1.5}O_4$ battery

[1]Department of Chemical System Engineering, The University of Tokyo, Tokyo, Japan. [2]Sungkyunkwan University Institute of Energy Science & Technology (SIEST), Sungkyunkwan University, Suwon-si, Korea. ✉e-mail: yamada@chemsys.t.u-tokyo.ac.jp

system offers low cost, high sustainability and high theoretical energy density (~610 Wh kg^{-1}, based on a negative/positive (N/P) ratio of 1), compared with those of commercial LIBs (~475 Wh kg^{-1}) with graphite anodes and LiCoO$_2$ cathodes (theoretically 274 mAh g^{-1}, but practically ~190 mAh g^{-1} with an average operating potential of ~3.9 V versus Li/Li$^+$ due to inevitable structural collapse)[6–9]. Also, it does not require change of the battery fabrication processes currently used. However, the realization of this promising battery system has been limited by severe electrolyte decomposition at the anode and cathode surfaces because the reaction (lithiation/delithiation) potentials of SiO$_x$ (≤0.4 V versus Li/Li$^+$) and LiNi$_{0.5}$Mn$_{1.5}$O$_4$ (≥4.7 V versus Li/Li$^+$) are outside the operating potential windows of existing electrolytes[10,11].

To address this problem, functional electrolytes and electrolyte additives have been developed over the past decades. These materials provide wide potential windows and form passivation films (solid electrolyte interphases (SEIs)) on the anode surfaces, kinetically retarding electrolyte degradation by blocking direct contact between the electrode and electrolyte. For instance, ether-based (such as 1,2-dimethoxyethane (DME) and tetrahydrofuran)[12,13] and fluorinated solvent-based electrolytes (such as fluoroethylene carbonate (FEC))[14,15] were applied to improve the reversibilities of SiO$_x$ and LiNi$_{0.5}$Mn$_{1.5}$O$_4$, respectively. Nevertheless, to the best of our knowledge, a stable SiO$_x$|LiNi$_{0.5}$Mn$_{1.5}$O$_4$ battery has not been realized due to the absence of electrolytes that provide high redox stabilities.

To establish a design strategy, the thermodynamic shift of lithiation/delithiation potential of SiO$_x$, which is dominated by the chemical potential of Li$^+$ in the electrolyte, should be highlighted as a critical factor in the reduction stability of the electrolyte[16–19]. The reductive decomposition of the electrolyte at the SiO$_x$ anode, in particular, can be largely suppressed by upshifting its inherent lithiation/delithiation potential, reducing the thermodynamic driving force of electrolyte reduction and thus unburdening the kinetic support of the SEI[20,21]. However, this strategy is yet to be applied to high-voltage batteries because the mechanisms behind the potential shift remain unclear, although the redox potential of an electrode depends on the electrolyte[16–19]. Recently, our group reported that the chemical potential of Li$^+$ increases in an ion-dense (Li$^+$–Li$^+$ and Li$^+$–anion) environment[22,23]. The progressive formation of ion-pair aggregates contributes to an upward shift in the redox potential of an electrode, thus thermodynamically mitigating the electrolyte decomposition at the electrode surface. Critically, the potentials of Li$^+$-related reactions (such as alloying and intercalation) shift by magnitudes that are identical to that of the redox potential of Li/Li$^+$. The substantial parallel shift (~0.6 V) cannot be observed in a typical (two-electrode) battery system and has thus been overlooked in the development and design of electrolytes and batteries[22,23].

Another critical factor is the protection of the SiO$_x$ surface with a highly Li$^+$-conductive and mechanically/chemically stable SEI[24,25]. The lithiation/delithiation of SiO$_x$ accompanies a considerable change in volume of up to 200% (ref. 7), causing severe damage not only to the SiO$_x$ particles, but also to the surface SEI layer. This accelerates electrolyte degradation by continuously exposing the electrode surface to the electrolyte[24–26]. Therefore, completely covering the SiO$_x$ surface with a robust SEI is essential in ensuring stable cycling with minimal electrolyte decomposition.

Considering these two crucial factors (Li/Li$^+$ potential upshift and advanced SEI formation), we report on the stable operation of a SiO$_x$|LiNi$_{0.5}$Mn$_{1.5}$O$_4$ battery over 1,000 cycles with an upper cut-off voltage of 4.9 V realized by optimizing its overall potential diagram in a strategically designed 3.4 mol L^{-1} (M) LiN(SO$_2$F)$_2$ (LiFSI)/methyl (2,2,2-trifluoroethyl) carbonate (FEMC) electrolyte. This electrolyte exhibits unique thermodynamic and kinetic characteristics. It features upshifting of the reaction potential of the SiO$_x$ anode, which is essential to reduce the thermodynamic driving force of electrolyte reduction. The electrolyte enables formation of a robust anion-derived
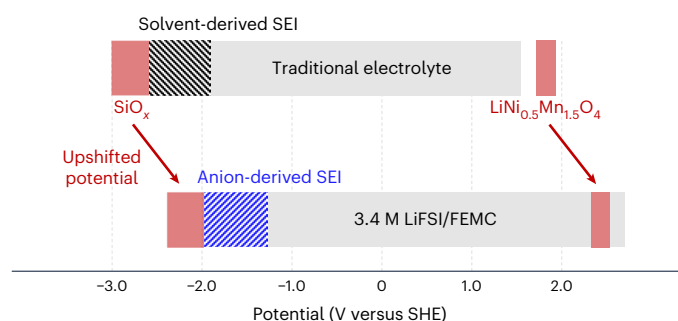
Fig. 1 | Potential diagram used in realizing the stable operation of SiO$_x$|LiNi$_{0.5}$Mn$_{1.5}$O$_4$ batteries with 3.4 M LiFSI/FEMC. For a comparison, the scenario of a SiO$_x$|LiNi$_{0.5}$Mn$_{1.5}$O$_4$ battery with a traditional carbonate-based electrolyte is included.

passivation film on the SiO$_x$ anode surface with tuned electronic states of anions. Additionally, high electrochemical stability can be realized for a high-potential LiNi$_{0.5}$Mn$_{1.5}$O$_4$ cathode, and degradation at high potentials, such as aluminium (Al) corrosion and transition metal dissolution from the cathode, can be suppressed.

Results

Concept of electrolyte design

Figure 1 represents the optimized potential diagram of a highly sustainable high-energy-density battery system, combined with a high-capacity, Earth-abundant SiO$_x$ anode and a high-potential, Co-free spinel LiNi$_{0.5}$Mn$_{1.5}$O$_4$ cathode in 3.4 M LiFSI/FEMC electrolyte. The stabilization mechanisms of the SiO$_x$ anode in 3.4 M LiFSI/FEMC include thermodynamic (upshifted potential) and kinetic (formation of SEI) factors. The upshifted electrode potential of SiO$_x$ aids in unburdening the kinetic support of the SEI, and, furthermore, the anion-derived SEI suppresses electrolyte decomposition more effectively. Notably, the upshifts in the electrode potentials of the SiO$_x$ anode and LiNi$_{0.5}$Mn$_{1.5}$O$_4$ cathode are identical, thus maintaining the overall battery voltage (Supplementary Note 1) while sustaining the electrode potential of the LiNi$_{0.5}$Mn$_{1.5}$O$_4$ cathode within the potential window of 3.4 M LiFSI/FEMC.

To optimize the overall potential diagram of the SiO$_x$|LiNi$_{0.5}$Mn$_{1.5}$O$_4$ battery, the electrolyte, 3.4 M LiFSI/FEMC, was designed as follows. The LiFSI salt was used due to its high solubility and capacity to form a robust anion-derived SEI[27,28]. FEMC was used as the solvent because the fluoro moiety increased the potential of solvent oxidation[14,29]. In addition, it reduced the negative partial charges on the oxygen atoms in the carbonate[30,31], weakening Li$^+$(solvent)$_n$ solvation and promoting the formation of more Li$^+$–anion ion pairs[32,33]. Finally, the salt concentration was increased to realize a peculiar solution structure, wherein Li$^+$ and FSI$^-$ ions were strongly coordinated and formed a congested ion-pair network, yielding several advantageous features.

First, extensive formation of the ion-pair network destabilizes Li$^+$ in the electrolyte (increases the chemical potential of Li$^+$) and upshifts the reaction potential of SiO$_x$, reducing the thermodynamic driving force of electrolyte reduction and thus unburdening the kinetic support of the SEI (Fig. 1)[22,23]. Second, the ion-pair-dominated solution structure provides a large amount of anions with modified electronic states[34], enabling the formation of a highly Li$^+$-conductive, mechanically/chemically stable anion-derived SEI on the negatively charged SiO$_x$ surface[35–37]. This advanced SEI effectively suppresses further electrolyte degradation at the SiO$_x$ surface (Fig. 1). Finally, several technical issues encountered at the positive LiNi$_{0.5}$Mn$_{1.5}$O$_4$ electrode under a high potential, such as electrolyte oxidation, Al corrosion and transition metal dissolution, are highly suppressed in 3.4 M LiFSI/FEMC by the increased potential of solvent oxidation and weak solvation capacity
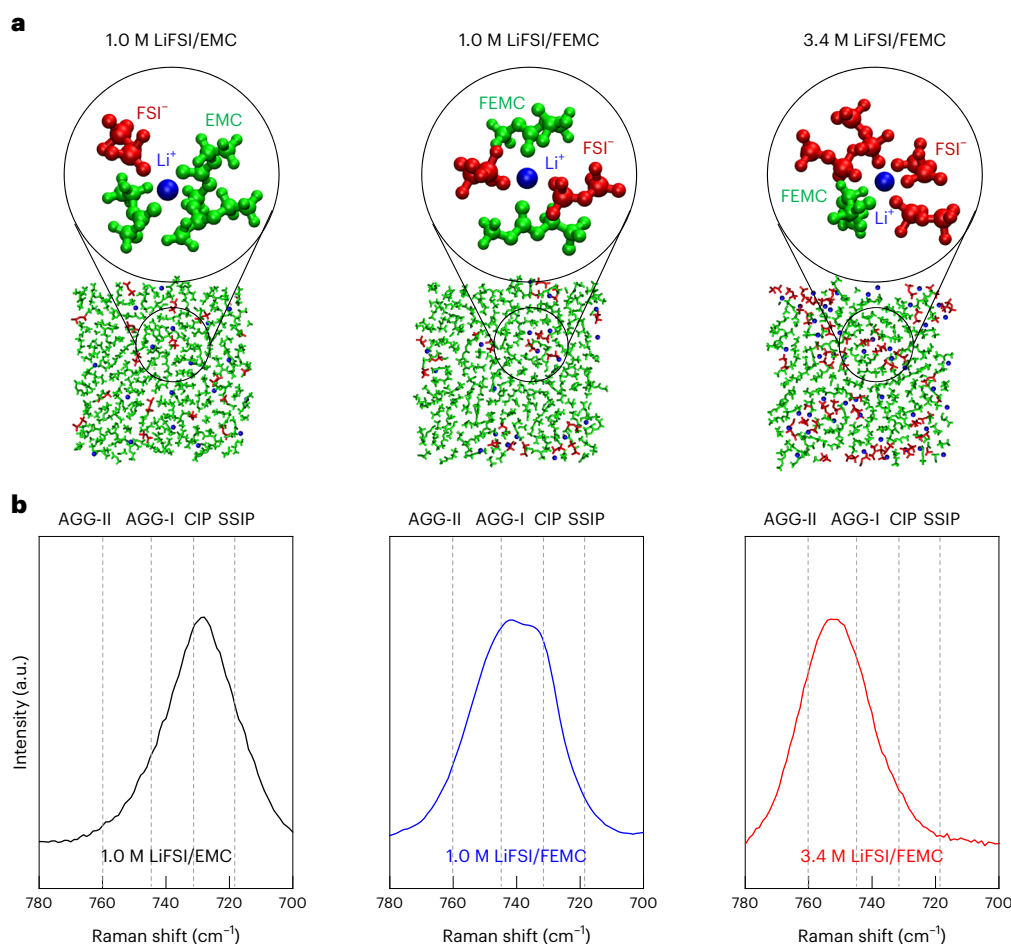
Fig. 2 | Electrolyte structures. a, Representative solution structures of 1.0 M LiFSI/EMC, 1.0 M LiFSI/FEMC and 3.4 M LiFSI/FEMC, as calculated via MD simulations. **b**, Raman spectra of the prepared electrolytes. The peak between 700 and 780 cm⁻¹ corresponds to the coordination environment of the FSI⁻ anion.

of the electrolyte[14,29,30,38,39]. Overall, high-level redox stabilities should be observed.

The design strategy of the electrolyte structure was verified via molecular dynamics (MD) simulations. The calculated solution structures of 1.0 M LiFSI/ethyl methyl carbonate (EMC), 1.0 M LiFSI/FEMC and 3.4 M LiFSI/FEMC are shown in Fig. 2a. The solution structure of the electrolyte changes drastically with the salt concentration and introduction of FEMC. For instance, Li^+ is surrounded by three or four EMC solvent molecules and one FSI^- anion in 1.0 M LiFSI/EMC. In contrast, multiple Li^+ and FSI^- ions are coordinated together while forming a closely packed ion-pair network in 3.4 M LiFSI/FEMC. The position of the primary peak in the radial distribution function $g(r)$ of Li^+–Li^+ shifts to a lower distance and the intensities of $g(r)$ for Li^+–Li^+ and Li^+–O_{FSI}^- are largely increased in 3.4 M LiFSI/FEMC (Supplementary Fig. 1). The solution structures of the electrolytes were also evaluated via Raman spectroscopy (Fig. 2b and Supplementary Fig. 2). The S–N–S stretching vibrational mode of FSI^- is considerably upshifted from 728 to 740 cm⁻¹ via the replacement of EMC with FEMC, indicating that the coordination states of FSI^- change from solvent-separated ion pairs (SSIP, bare FSI^- and/or FSI^- solvated with solvent molecules) and contact ion pairs (CIP, FSI^- coordinated to one Li^+) to ion-pair aggregates (AGG-I and AGG-II, where more than two FSI^- and Li^+ ions coordinate while forming an ion-pair network)[40]. The peak position is further upshifted to 752 cm⁻¹ with increasing salt concentration. Thus, the computational and experimental studies suggest that the 3.4 M LiFSI/FEMC electrolyte displays an ion-pair aggregate-dominated solution structure.

Suppression of reductive degradation

Figure 3a shows the charge–discharge curves and cycling stabilities of Li|SiO_x half-cells in three electrolytes, that is, 1.0 M LiFSI/EMC, 1.0 M LiFSI/FEMC and 3.4 M LiFSI/FEMC. The studies were conducted using a slow current of 150 mA g⁻¹, requiring >3 months for 80 cycles, to carefully evaluate the reduction stabilities of the electrolytes on the SiO_x surface. A stable cycling of Li|SiO_x under such slow and long duration has been rarely reported because slow cycling exacerbates the electrolyte decomposition on the SiO_x surface[7,9]. Even under such severe conditions, 93% of the capacity is retained after 80 cycles in 3.4 M LiFSI/FEMC, which is much higher than the capacity retentions in 1.0 M LiFSI/EMC (19% after 80 cycles) and 1.0 M LiFSI/FEMC (85% after 80 cycles). A similar trend is observed in the galvanostatic Li plating/stripping test, wherein the 3.4 M LiFSI/FEMC electrolyte exhibits a substantially higher Coulombic efficiency (~97%) than that of 1.0 M LiFSI/EMC (≤60%; Supplementary Fig. 4). The optimal performance is observed using the 3.4 M LiFSI/FEMC electrolyte designed in this study.

As a crucial factor influencing the reversibility, we focused on the redox potential of Li/Li⁺ (the lowest possible reaction potential of SiO_x), which should correlate closely with the degree of reductive electrolyte decomposition[22]. Cyclic voltammetry (CV) was performed with an International Union of Pure and Applied Chemistry (IUPAC)-recommended electrolyte-independent redox system (ferrocene, Fc/Fc⁺) as a reference electrode to estimate the redox potentials of Li/Li⁺ (and thus the reaction potentials of SiO_x) in various electrolytes[41,42]. As shown in Supplementary Fig. 5, the respective redox potentials of ferrocene are 3.25, 3.07 and 2.91 V versus Li/Li⁺ in 1.0 M LiFSI/EMC, 1.0 M LiFSI/FEMC
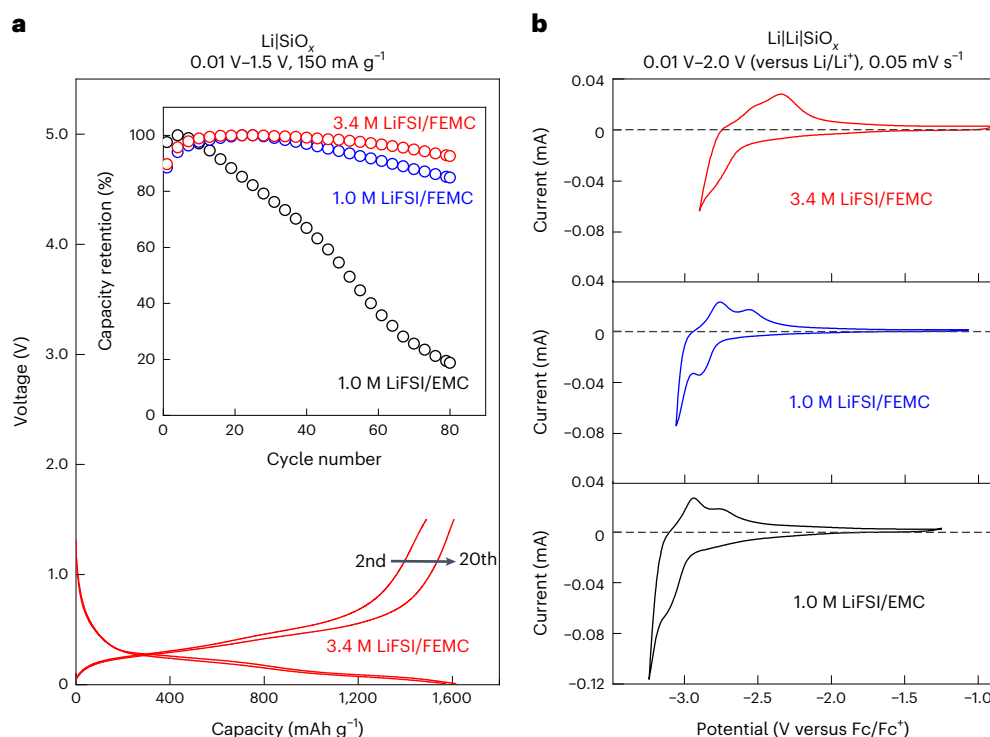
Fig. 3 | Improved cycling stability of SiO_x with its potential upshift. a, Charge and discharge curves of a Li|SiO_x half-cell in the 3.4 M LiFSI/FEMC electrolyte. The inset shows the capacity retention of cells with various electrolytes as a function of the cycle number. The first charge and discharge curves and Coulombic efficiencies of the Li|SiO_x half-cells in the prepared electrolytes are shown in Supplementary Fig. 3. **b**, Cyclic voltammograms of the SiO_x anode in the prepared electrolytes. The reaction potentials of SiO_x were calibrated based on ferrocene, which is an IUPAC-recommended electrolyte-independent redox complex (Supplementary Fig. 5)[41,42]. The increase in capacity during the initial cycles of the Li|SiO_x cells may be ascribed to the stabilization (activation) of the SiO_x anodes, involving their bulk and surface reconstruction via complex interactions between the binder, active material and electrolyte[50,51].

and 3.4 M LiFSI/FEMC. Correspondingly, the redox potential of Li/Li$^+$ (V versus Fc/Fc$^+$) is considerably upshifted by 0.34 V in 3.4 M LiFSI/FEMC relative to that in 1.0 M LiFSI/EMC (Fig. 3b and Supplementary Fig. 5).

This remarkable thermodynamic variation in the redox potential is due to the chemical potential (stability) of Li$^+$ in the electrolyte[22,23]. As shown in Fig. 2 and Supplementary Fig. 1, the 3.4 M LiFSI/FEMC electrolyte exhibits a unique solution structure, wherein most Li$^+$ and FSI$^-$ ions are extensively coordinated to form a dense ion-pair network. This configuration drastically destabilizes Li$^+$ in the electrolyte (Supplementary Fig. 6), resulting in simultaneous upshifts of identical magnitudes of the redox potentials of the anode and cathode[22,23]. Notably, the burden of the SEI can be largely mitigated by reducing the thermodynamic driving force of electrolyte reduction with the upshifted reaction potential[20,21]. Indeed, the 3.4 M LiFSI/FEMC electrolyte, which exhibits a redox potential of Li/Li$^+$ that is 0.6 V higher (−2.91 V versus Fc/Fc$^+$) than that of 1.0 M LiFSI/diglyme (−3.48 V versus Fc/Fc$^+$), provides a considerably enhanced stability (Supplementary Figs. 5 and 7).

Consequently, the considerably upshifted redox potential of Li/Li$^+$ (and thus, simultaneously upshifted reaction potential of SiO_x) in 3.4 M LiFSI/FEMC unburdens the kinetic support of the SEI, contributing to the decrease in the reductive decomposition of the electrolyte at the SiO_x surface.

In addition to the thermodynamic upshift of the electrode potential, kinetic hindrance of electrolyte decomposition by the SEI should be considered[35,43]. This is because the reaction potential of the SiO_x anode remains outside the thermodynamic potential window of the electrolyte, although the burden of the SEI kinetic support is decreased via the upshifting of the electrode potential in 3.4 M LiFSI/FEMC. In this respect, X-ray photoelectron spectroscopy (XPS) of the cycled SiO_x electrodes was performed. Large amounts of various functionalities (Li−F, S−O−F, S=O and S−S) are detected on the SiO_x surface in 3.4 M

LiFSI/FEMC (Fig. 4a), indicating that the FSI$^-$ anions are progressively decomposed[34]. This aids in forming an inorganic-rich SEI, which provides a high ionic conductivity and mechanical/chemical stability[35–37]. According to the electrochemical impedance spectroscopy (EIS), a low interfacial resistance is maintained upon cycling and the signals representing the damage of SEI on the SiO_x surface are undetected in 3.4 M LiFSI/FEMC even after 50 cycles (Fig. 4b,c and Supplementary Fig. 8). Such a substantial stabilization is not observed using 1.0 M LiFSI/EMC.

Overall, stable cycling of the SiO_x anode is thermodynamically (upshifted electrode potential) and kinetically (anion-derived SEI) realized using 3.4 M LiFSI/FEMC, which is due to its distinct solution structure.

Improved oxidative stability

After confirming that the unique coordination environments of Li$^+$ and FSI$^-$ in 3.4 M LiFSI/FEMC result in the high reversibility of the SiO_x anode, we evaluated the oxidative stability of the electrolyte. Most electrolytes developed for use with Si-based anodes are not used with high-potential cathodes because of the poor oxidative stabilities of the electrolytes[7,10]. However, the 3.4 M LiFSI/FEMC electrolyte enables the stable operation of a Li|LiNi$_{0.5}$Mn$_{1.5}$O$_4$ half-cell (≥90% capacity retention after 100 cycles with an average Coulombic efficiency of ~99%) with an upper cut-off potential of 4.9 V at a low constant C rate of 0.2C, which is impossible in 1.0 M LiFSI/EMC (continuous oxidative decomposition at 4.5 V versus Li/Li$^+$) and 1.0 M LiFSI/FEMC (78% capacity retention after 100 cycles with a poor Coulombic efficiency of <90%; Fig. 5a and Supplementary Fig. 9). This indicates that the 3.4 M LiFSI/FEMC electrolyte can deliver a wide operating potential window covering those of the Co-free, high-potential LiNi$_{0.5}$Mn$_{1.5}$O$_4$ cathode and high-capacity, low-potential SiO_x anode on the basis of a combination of thermodynamic and kinetic effects.

a SiO$_x$ electrodes after 1 cycle

b Si 2p spectra of SiO$_x$ electrodes

c
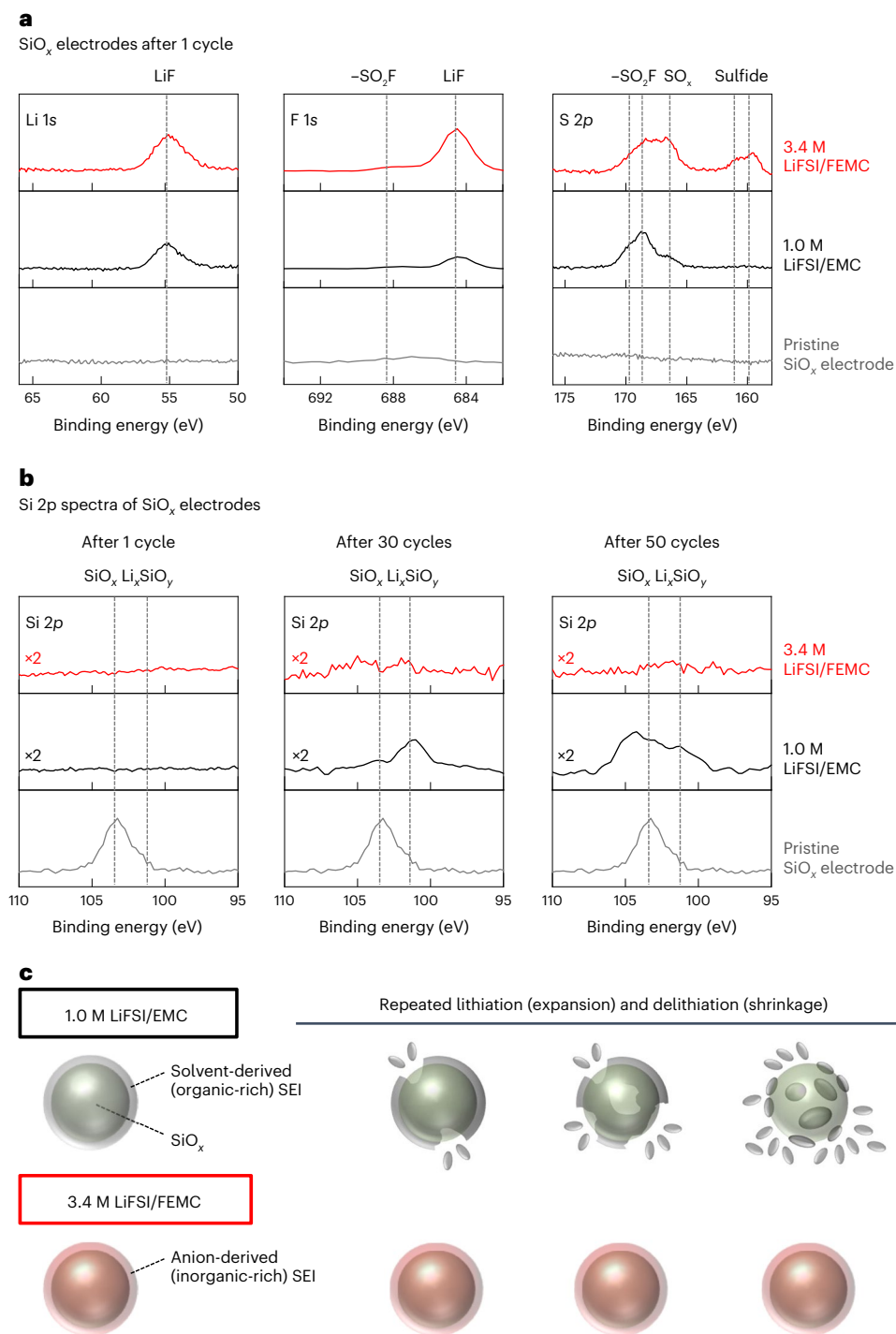
Fig. 4 | Passivation of the SiO$_x$ surface. a,b, Li 1s, F 1s, S 2p (**a**) and Si 2p (**b**) XPS spectra of the SiO$_x$ electrodes cycled in 1.0 M LiFSI/EMC and 3.4 M LiFSI/FEMC. **c**, Schematic diagram of the SEI stability on cycling in electrolytes with different compositions.

Linear sweep voltammetry (LSV) was performed to investigate the anodic limits of the electrolytes and their tolerance against Al corrosion, using Pt or Al as the working electrode. The anodic current flow on Pt was initiated at >5.3 V (versus Li/Li$^+$) in 1.0 and 3.4 M LiFSI/FEMC electrolytes, which was higher than that in 1.0 M LiFSI/EMC (4.7 V versus Li/Li$^+$), thus including the upper cut-off potential of the LiNi$_{0.5}$Mn$_{1.5}$O$_4$ cathode (4.9 V versus Li/Li$^+$; Fig. 5a,b). This trend is consistent with an increase in the oxidative stability of the electrolyte upon introducing the electron-withdrawing F groups[14,29]. Noticeably, Al corrosion is not observed at ≤5.8 V (versus Li/Li$^+$) in 3.4 M LiFSI/FEMC, whereas it commences at <4.5 V (versus Li/Li$^+$) in 1.0 M LiFSI/EMC and 1.0 M LiFSI/FEMC (Fig. 5c). Al corrosion occurs with the formation of Al^{3+}(solvent)$_n$ solvates and/or Al(anion)$_n$ complexes, followed by their diffusion into the bulk electrolyte[38]. However, such solvates are hardly formed in 3.4 M LiFSI/FEMC owing to the weak solvating power of FEMC[30]. Moreover, the diffusion of Al^{3+} complexes into the bulk electrolyte is kinetically retarded because of the poor dissolution capacity of the ion-pair-congested electrolyte[39]. Floating tests with carbon electrodes, which provide the largest surface areas of the cathode composites as conductive additives, also indicate the high oxidative
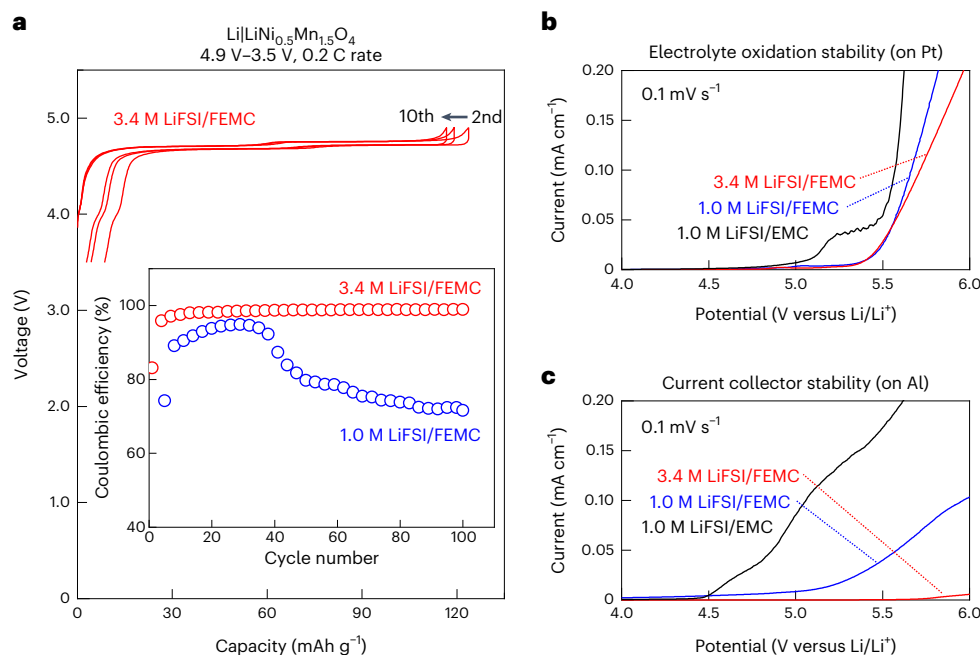
Fig. 5 | Stable cathode operation at a high potential. a, Charge and discharge curves of the Li|LiNi$_{0.5}$Mn$_{1.5}$O$_4$ half-cell with 3.4 M LiFSI/FEMC. The inset shows the Coulombic efficiencies of the cells with the prepared electrolytes as a function of the cycle number. The first charge and discharge curves are shown in Supplementary Fig. 9. **b,c**, Oxidative stabilities of the electrolytes on Pt (**b**) and corrosion stabilities of the Al current collector (**c**) in the three electrolytes. The origin of low initial Coulombic efficiency can be a passivation film (SEI and CEI) formation (Fig. 4 and Supplementary Fig. 10).

stability of 3.4 M LiFSI/FEMC at >5.0 V versus Li/Li$^+$ (Supplementary Fig. 11). The solvent fluorination, weak solvating power and unique solution structure improve the oxidative stability of the electrolyte and prevent Al corrosion in a thermodynamic (increased potential of solvent oxidation) and kinetic (impeded generation and diffusion of Al^{3+} solvates and complexes) manner.

Highly stable SiO$_x$|LiNi$_{0.5}$Mn$_{1.5}$O$_4$ batteries

Before assembling full SiO$_x$|LiNi$_{0.5}$Mn$_{1.5}$O$_4$ coin-type cells with 3.4 M LiFSI/FEMC electrolytes, the SiO$_x$ electrodes were pre-activated to compensate their inherently large irreversible capacities in the initial cycles (Supplementary Fig. 12)[7]. Notably, pre-activation does not mean full lithiation, which provides a large amount of additional Li source to the cell. The cycling stabilities of the pre-activated full SiO$_x$|LiNi$_{0.5}$Mn$_{1.5}$O$_4$ cells with average operating voltages of 4.3 V under upper cut-off voltages of 4.9 V at low constant C rates of 0.2C in various electrolytes are shown in Supplementary Fig. 13. Notably, 85% of the maximum capacity is maintained after 300 cycles in 3.4 M LiFSI/FEMC, whereas the cell performance declines drastically in 1.0 M LiFSI/EMC (continuous oxidative decomposition upon charging), 1.0 M LiFSI/FEMC (56% after 100 cycles) and commercial 1.0 M LiPF$_6$/ethylene carbonate:dimethyl carbonate (EC:DMC, 1:1, v/v, 56% after 300 cycles). A negligible capacity decay is observed in 3.4 M LiFSI/FEMC at a constant C rate of 0.5C over 500 cycles, with a Coulombic efficiency of ~100% (Fig. 6). Moreover, the cycling study conducted under harsh conditions of 55 °C reveals a considerably improved cycling stability (72% capacity retention after 300 cycles) in 3.4 M LiFSI/FEMC compared to that in 1.0 M LiPF$_6$/EC:DMC (1:1, v/v, 52% after 100 cycles; Supplementary Fig. 14). The result of energy-dispersive X-ray spectroscopy (EDX) reveals negligible amounts of Mn and Ni on the SiO$_x$ anode cycled in the full-cell with 3.4 M LiFSI/FEMC, indicating that transition metal dissolution from the cathode is highly suppressed due to the unique solution structure and weak solvating power of the electrolyte (Supplementary Fig. 15)[14,29,30,38,39]. This is in contrast to that obtained using 1.0 M LiPF$_6$/EC:DMC (1:1, v/v), which exhibits severe transition metal dissolution. In addition, highly reproducible long-term cycling of full-cells over 1,000 cycles under practical battery conditions (high-loading-level cathodes, limited amounts of electrolytes with standard electrolyte additives) supports the high redox stabilities of 3.4 M LiFSI/FEMC (Supplementary Figs. 16 and 17).

In conclusion, 3.4 M LiFSI/FEMC provides unusual stabilities at the SiO$_x$ anode and LiNi$_{0.5}$Mn$_{1.5}$O$_4$ cathode, which are incomparable to those of other electrolytes proposed so far (Fig. 6b).

Discussion

Stable long-term cycling of high-energy-density yet sustainable SiO$_x$|LiNi$_{0.5}$Mn$_{1.5}$O$_4$ batteries over 1,000 cycles was realized with 3.4 M LiFSI/FEMC electrolytes by optimizing the overall potential diagram of the full-cell. The solution structure of 3.4 M LiFSI/FEMC was distinct, with most Li$^+$ and FSI$^-$ ions extensively coordinated to form a dense ion-pair network. This destabilized Li$^+$ in the electrolyte and enabled a large amount of the anion with a modified electronic state to approach the negatively charged SiO$_x$ anode. This contributed to the stable cycling of the SiO$_x$ anode by upshifting the thermodynamic reaction potential of SiO$_x$ and forming a highly functional anion-derived SEI. Moreover, several problems induced by the high-potential cathode could be resolved because of the thermodynamically enhanced oxidative stability and the kinetically prevented Al corrosion and transition metal dissolution from the cathode composites. These advanced functionalities were due to the increased potential of solvent oxidation and weakened solvating power with solvent fluorination and poor dissolution capacity of the electrolyte.

It is important to note that while the proposed electrolyte strategy in this paper is expected to promote the utilization of economic and green electrode materials, challenges still remain for the commercialization of next-generation battery systems. Further optimization and development of electrode composition and cell design, including thin separators with high oxidation and reduction stabilities, high oxidation-tolerant carbon additives with high electrical conductivity and advanced binders and functional electrolyte additives passivating
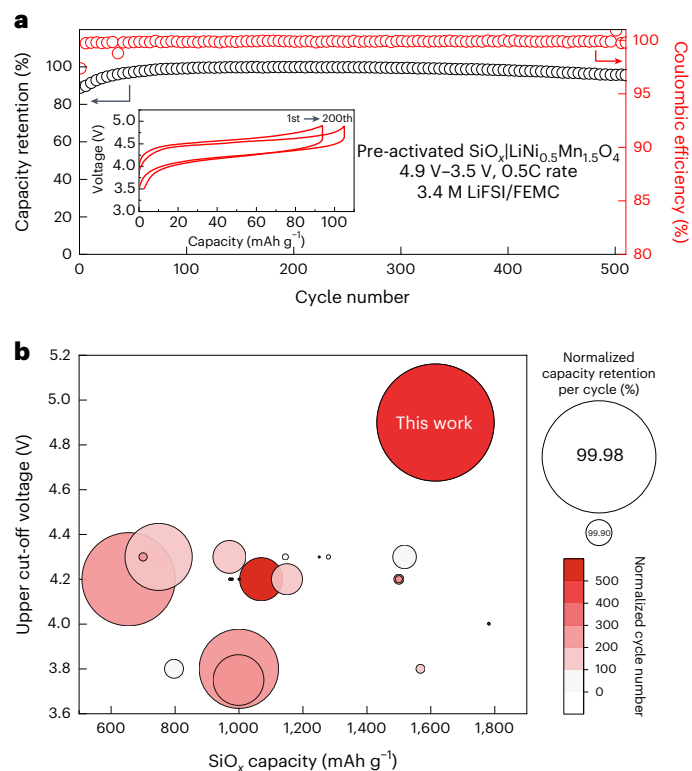
Fig. 6 | Excellent long-term stability of a full SiO$_x$|LiNi$_{0.5}$Mn$_{1.5}$O$_4$ cell.
a, Discharge capacity retention of the pre-activated full SiO$_x$|LiNi$_{0.5}$Mn$_{1.5}$O$_4$ cell with an upper cut-off voltage of 4.9 V at a low constant C rate of 0.5C in 3.4 M LiFSI/FEMC as a function of the cycle number. Every fifth point is plotted, and the inset shows the charge and discharge curves of the full-cell. The capacity was calculated on the basis of the weight of the cathode active materials.
b, Comparison of the performance with those of previously reported full-cells with SiO$_x$ anodes. The plot shows four parameters: the capacity of the SiO$_x$ anodes (x axis), upper cut-off voltages of the full-cells (y axis), cycle numbers of the full-cells (colour depth) and capacity retention of the full-cells per cycle (diameter, with capacity retention improving with increasing diameter). The details of the literature data and normalization are described in Supplementary Tables 3 and 4 (refs. 52–71). Note that most previous reports are based on coin-cell studies, and our experimental conditions are most severe for achieving better cycling performance (high electrode loading, limited electrolyte volume, slow C rates and high cut-off voltages), as detailed in Supplementary Table 3. The full-cell and rate performances with high-loading-level cathodes and electrolyte additives are also shown in Supplementary Figs. 16–18.

electrodes, along with devising battery pack designs to improve overall battery safety, will help to enhance battery performance under various operating conditions (low and high temperatures, fast charge, deep discharge and so on), thus facilitating the realization of highly sustainable high-energy-density batteries.

Methods

Electrolytes
The electrolytes were prepared using a LiFSI salt (Nippon Shokubai) and solvents (EMC, Kishida Chemical; FEMC, Halocarbon) and diglyme (Kishida Chemical) in an Ar-filled glovebox. The commercial 1.0 M LiPF$_6$/EC:DMC (1:1, v/v) electrolyte was purchased from Kishida Chemical and used as received.

SiO$_x$ electrode
SiO$_x$ (BTR New Energy Material), acetylene black (AB, Denka Black Li-400, Denka) and polyamide-imide binder (PAI, Torlon-4000T, Solvay) were dissolved in N-methylpyrrolidone (NMP, FUJIFILM Wako Pure Chemical) in a mass ratio of 70:15:15. The prepared slurry was

coated onto a Cu foil (Fchikawa Rare Metal) and dried at 80 °C in an oven. The resulting electrode was further heated at 400 °C for 2 h in an Ar atmosphere to strengthen the mechanical stability of the PAI binder[44].

LiNi$_{0.5}$Mn$_{1.5}$O$_4$ electrode
LiNi$_{0.5}$Mn$_{1.5}$O$_4$ (Samsung SDI), AB or blended carbons (AB and graphitized Ketjen black (FD7010, Lion Specialty Chemicals)) and polyvinylidene fluoride (PVDF) or lithiated polyacrylic acid (LiPAA) binder were mixed in NMP or water in a mass ratio of 80:10:10 or 85:10:5 or 80:15:5. The obtained viscous slurry was cast onto an Al (Fchikawa Rare Metal) or carbon-coated Al foil (SDX-PM, Showa Denko) and then dried at 80 °C in an oven. LiPAA was prepared by titrating an aqueous solution of PAA (FUJIFILM Wako Pure Chemical) with LiOH (FUJIFILM Wako Pure Chemical) until the pH of the solution was 7 (ref. 45).

Electrochemical study
The 2032 coin-type cell components were purchased from Hohsen, and all cell components and SiO$_x$ and LiNi$_{0.5}$Mn$_{1.5}$O$_4$ electrodes were dried at 200 or 120 °C under vacuum before use[46]. The coin-type half- and full-cells were assembled in an Ar-filled glovebox under the supplied conditions. Cellulose (Nippon Kodoshi) and polypropylene membranes (Celgard) and glass fibre filters (Advantec) were used as separators. The galvanostatic charge and discharge studies were performed at various temperatures using a charge–discharge instrument (TOSCAT-3100, Toyo System).

The SiO$_x$ electrodes of the full-cells were pre-activated to compensate for Li consumption upon their initial activation[7]. Initially, a Li|SiO$_x$ half-cell was fabricated and cycled (lithiated and delithiated) once in the potential range 0.01–1.5 V. Subsequently, it was relithiated for 30–40 min at a constant current of 150 mA g^{-1} in the prepared electrolyte (1.0 M LiFSI/EMC, 1.0 M LiFSI/FEMC, 3.4 M LiFSI/FEMC or 1.0 M LiPF$_6$/EC:DMC (1:1, v/v)) to prevent corrosion of the Cu current collector. The capacity ratio of the lithiated pre-activated SiO$_x$ electrode was approximately 5%. Finally, the pre-activated SiO$_x$ electrode was carefully collected from the cell and reassembled with fresh electrolyte.

The pre-activated full SiO$_x$|LiNi$_{0.5}$Mn$_{1.5}$O$_4$ cell, as shown in Fig. 6, was fabricated using a LiNi$_{0.5}$Mn$_{1.5}$O$_4$ electrode (loading level of 5 mg cm^{-2}), pre-activated SiO$_x$ and the 3.4 M LiFSI/FEMC electrolyte. A glass fibre filter was used as the separator, and the N/P ratio was controlled at 1.4. The N/P ratio and C rate were calculated using the capacities of LiNi$_{0.5}$Mn$_{1.5}$O$_4$ (147 mAh g^{-1}) and SiO$_x$ (1,500 mAh g^{-1}). The cell was cycled ten times at a C rate of 0.2C to stabilize the SEI before applying a C rate of 0.5C. In every half- and full-cell study, 80 µl of electrolyte was used, except those shown in Supplementary Figs. 16 and 17, wherein 40 µl was used to simulate the practical battery condition. The electrode and cell data of other half- and full-cells are provided in the figure captions.

Coulombic efficiency is defined as the percentage of the discharge capacity at the nth cycle divided by the charge capacity at the nth cycle (that is, the ratio between the number of electrons transferred from the cathode to the anode during charging and the number transferred back during discharging).

Capacity retention is defined as the percentage of the discharge capacity at the nth cycle divided by the maximum discharge capacity over all cycles. Unidentifiably slight side reactions hindered by an electrolyte-rich condition in the coin cell might have led to an observation of better capacity retention than the expected value based on the Coulombic efficiency (Supplementary Figs. 16 and 17)[47]. Despite this unavoidable minor error, the present results still establish an important benchmark for stable operation of the SiO$_x$|LiNi$_{0.5}$Mn$_{1.5}$O$_4$ system, as evidenced by its distinctiveness in the relative comparison provided in Fig. 6.

The redox potential of Li/Li$^+$ was estimated via CV using a three-electrode cell (Pt|Li|Li) in the given electrolytes with ~1 mM of the IUPAC-recommended electrolyte-independent redox system

(Fc/Fc$^+$). CV was performed at a scan rate of 5 mV s^{-1}. Cyclic voltammograms illustrated in the figure in Supplementary Note 1 were obtained using a three-electrode cell consisting of a working electrode (SiO$_x$ or Li$_4$Ti$_5$O$_{12}$ or LiFePO$_4$ or LiNi$_{0.5}$Mn$_{1.5}$O$_4$ electrode) and Li metal as the counter and reference electrodes with given electrolytes at a scan rate of 0.05 or 0.1 mV s^{-1}.

The galvanostatic Li plating/stripping study was conducted with half-cells (Li|Cu) in various electrolytes at a constant current density of 0.5 mA cm^{-2} and an areal capacity of 0.5 mAh cm^{-2} with a cut-off voltage of 0.5 V. The deposited diameter of Li on the Cu foil was 1.2 cm.

The interfacial resistance between the electrode and electrolyte in a cycled half-cell (Li|SiO$_x$) in its fully discharged state was analysed using EIS (VMP3 potentiostat, BioLogic), with an amplitude of 10 mV over the frequency range 10 mHz to 1 MHz.

The oxidative stabilities of the electrolytes and the Al corrosion in various electrolytes were investigated via LSV in a three-electrode cell with a Pt plate or an Al foil as the working electrode and Li metal as the counter and reference electrodes. LSV was performed using the VMP3 potentiostat from the open-circuit potential to 6 V (versus Li/Li$^+$) at a scan rate of 0.1 mV s^{-1}.

The floating test was conducted using conductive carbon additive/PVDF binder (1:1, w/w) electrodes coated on Al current collectors as the working electrodes and Li metal as the counter and reference electrodes from 4.0 to 5.6 V versus Li/Li$^+$.

Characterizations

The basic physicochemical properties of the prepared electrolytes are shown in Supplementary Table 1. The densities and viscosities of the electrolytes were measured using an oscillator-type densitometer (DMA 35, Anton Paar) and a viscometer (Lovis 2000 M, Anton Paar), respectively. The ionic conductivities of the electrolytes were evaluated in a two-electrode glass cell (Pt|electrolyte|Pt) via alternating-current impedance spectroscopy (Solartron 147055BEC, Solartron Analytical).

The solution structures of the electrolytes were analysed via Raman spectroscopy (NRS-5100, JASCO) at a laser excitation wavelength of 532 nm. The electrolyte was placed in a quartz cell, which was sealed with Parafilm in an Ar-filled glovebox to avoid air contamination.

The surface chemistry of the cycled SiO$_x$ and LiNi$_{0.5}$Mn$_{1.5}$O$_4$ electrodes was studied via XPS (PHI 5000 Versaprobe-II, ULVAC-PHI) with a monochromatic AlKα X-ray source. The samples were prepared by disassembling the cycled cells and then rinsing them several times with DME in an Ar-filled glovebox. The samples were then transferred into the XPS chamber without exposure to the air using a specially designed transfer vessel.

EDX of the SiO$_x$ electrodes was performed to estimate the amounts of dissolved transition metals originating from the cathode materials. The SiO$_x$ electrodes were carefully collected from the cycled full SiO$_x$|LiNi$_{0.5}$Mn$_{1.5}$O$_4$ cells under the provided conditions and then washed several times with DME before measurement.

Computational study

The MD simulations were conducted to estimate the electrolyte structures and stabilities of Li$^+$ (electrostatic potentials at the Li$^+$ sites) in the prepared electrolytes using the AMBER16 package. The details of the calculation model are shown in Supplementary Table 2, with the numbers of solvent molecules/ions based on the experimental compositions. The generalized AMBER force field[48] was used for all solvent molecules/ions in the simulations. The atomic point charges were obtained via gas-phase density functional theory calculations at the B3LYP/cc-pvdz level using the Gaussian 16 package. The time step was set to 1 fs using the SHAKE method[49], constraining the H−heavy atom bond distances. The simulation cells were adjusted using NPT-MD simulations at 1 bar and 298 K, followed by NVT-MD simulations (298 K) to equilibrate the system for 1 ns and subsequent sampling for 10 ns. The calculated solution structures were consistent with the data obtained via Raman spectroscopy (Fig. 2). The electrostatic potential was evaluated by summing all electrostatic interactions from the electrolyte solvent molecules/ions to each Li$^+$ ion using the particle mesh Ewald method under periodic boundary conditions and then averaging the obtained values.

Reporting summary

Further information on research design is available in the Nature Portfolio Reporting Summary linked to this article.

Data availability

All the relevant data are included in the paper and its Supplementary Information. The data that support the findings of this study are available from the corresponding author on reasonable request.

References

1. Gent, W. E., Busse, G. M. & House, K. Z. The predicted persistence of cobalt in lithium-ion batteries. *Nat. Energy* **7**, 1132–1143 (2022).
2. Manthiram, A. A reflection on lithium-ion battery cathode chemistry. *Nat. Commun.* **11**, 1550 (2020).
3. Banza, C. L. N. et al. Sustainability of artisanal mining of cobalt in DR Congo. *Nat. Sustain.* **1**, 495–504 (2018).
4. Olivetti, E. A., Ceder, G., Gaustad, G. G. & Fu, X. Lithium-ion battery supply chain considerations: analysis of potential bottlenecks in critical metals. *Joule* **1**, 229–243 (2017).
5. Lee, S. & Manthiram, A. Can cobalt be eliminated from lithium-ion batteries? *ACS Energy Lett.* **7**, 3058–3063 (2022).
6. Wang, J. et al. Superconcentrated electrolytes for a high-voltage lithium-ion battery. *Nat. Commun.* **7**, 12032 (2016).
7. Liu, Z. et al. Silicon oxides: a promising family of anode materials for lithium-ion batteries. *Chem. Soc. Rev.* **48**, 285–309 (2019).
8. Ryu, J., Hong, D., Lee, H. & Park, S. Practical considerations of Si-based anodes for lithium-ion battery applications. *Nano Res.* **10**, 3970–4002 (2017).
9. Xu, Z. et al. Silicon microparticle anodes with self-healing multiple network binder. *Joule* **2**, 950–961 (2018).
10. Eshetu, G. G. & Figgemeier, E. Confronting the challenges of next-generation silicon anode-based lithium-ion batteries: role of designer electrolyte additives and polymeric binders. *ChemSusChem* **12**, 2515–2539 (2019).
11. Fan, X. & Wang, C. High-voltage liquid electrolytes for Li batteries: progress and perspectives. *Chem. Soc. Rev.* **50**, 10486–10566 (2021).
12. Chen, J. et al. Electrolyte design for LiF-rich solid–electrolyte interfaces to enable high-performance microsized alloy anodes for batteries. *Nat. Energy* **5**, 386–397 (2020).
13. Cao, Z., Zheng, X., Qu, Q., Huang, Y. & Zheng, H. Electrolyte design enabling a high-safety and high-performance Si anode with a tailored electrode–electrolyte interphase. *Adv. Mater.* **33**, 2103178 (2021).
14. Zhang, Z. et al. Fluorinated electrolytes for 5 V lithium-ion battery chemistry. *Energy Environ. Sci.* **6**, 1806–1810 (2013).
15. Hu, L., Zhang, Z. & Amine, K. Fluorinated electrolytes for Li-ion battery: an FEC-based electrolyte for high voltage LiNi$_{0.5}$Mn$_{1.5}$O$_4$/graphite couple. *Electrochem. Commun.* **35**, 76–79 (2013).
16. Moon, H. et al. Mechanism of Li ion desolvation at the interface of graphite electrode and glyme-Li salt solvate ionic liquids. *J. Phys. Chem. C* **118**, 20246–20256 (2014).
17. Kottam, P. K. R., Kalkan, D., Wohlfahrt-Mehrens, M. & Marinaro, M. Influence of Li-salt concentration on redox potential of lithium metal and electrochemistry of ferrocene in DMSO-based electrolytes. *J. Electrochem. Soc.* **166**, A1574–A1579 (2019).
18. Yamada, Y. et al. Hydrate-melt electrolytes for high-energy-density aqueous batteries. *Nat. Energy* **1**, 16129 (2016).

19. Kim, S. C. et al. Potentiometric measurement to probe solvation energy and its correlation to lithium battery cyclability. *J. Am. Chem. Soc.* **143**, 10301–10308 (2021).

20. Steinrück, H.-G. Modeling cyclic voltammetry during solid electrolyte interphase formation: baseline scenario of a dynamically evolving tunneling barrier resulting from a homogeneous single-phase insulating film. *J. Chem. Phys.* **154**, 174703 (2021).

21. Kolzenberg, L., Latz, A. & Horstmann, B. Solid-electrolyte interphase during battery cycling: theory of growth regimes. *ChemSusChem* **13**, 3901–3910 (2020).

22. Ko, S. et al. Electrode potential influences the reversibility of lithium-metal anodes. *Nat. Energy* **7**, 1217–1224 (2022).

23. Takenaka, N., Ko, S., Kitada, A. & Yamada A. Liquid Madelung potential as a descriptor for lithium metal electrodes. Preprint at https://doi.org/10.21203/rs.3.rs-1830373/v1 (2022).

24. Yin, Y. et al. Nonpassivated silicon anode surface. *ACS Appl. Mater. Interfaces* **12**, 26593–26600 (2020).

25. Cao, C. et al. Solid electrolyte interphase on native oxide-terminated silicon anodes for Li-ion batteries. *Joule* **3**, 762–781 (2019).

26. Han, S. Y. et al. Stress evolution during cycling of alloy-anode solid-state batteries. *Joule* **5**, 2450–2465 (2021).

27. Yamada, Y. et al. Unusual stability of acetonitrile-based superconcentrated electrolytes for fast-charging lithium-ion batteries. *J. Am. Chem. Soc.* **136**, 5039–5046 (2014).

28. Yamada, Y., Wang, J., Ko, S., Watanabe, E. & Yamada, A. Advances and issues in developing salt-concentrated battery electrolytes. *Nat. Energy* **4**, 269–280 (2019).

29. Achiha, T. et al. Thermal stability and electrochemical properties of fluorine compounds as nonflammable solvents for lithium-ion batteries. *J. Electrochem. Soc.* **157**, A707 (2010).

30. Su, C.-C. et al. Solvating power series of electrolyte solvents for lithium batteries. *Energy Environ. Sci.* **12**, 1249–1254 (2019).

31. Yao, Y. et al. Regulating interfacial chemistry in lithium-ion batteries by a weakly solvating electrolyte. *Angew. Chem. Int. Ed. Engl.* **60**, 4090–4097 (2021).

32. Eilmes, A. Li$^+$ binding to fluorinated carbonate solvents studied by ab initio quantum chemical calculations. *J. Mol. Liq.* **224**, 452–459 (2016).

33. Hou, T. et al. The influence of FEC on the solvation structure and reduction reaction of LiPF$_6$/EC electrolytes and its implication for solid electrolyte interphase formation. *Nano Energy* **64**, 103881 (2019).

34. Sodeyama, K., Yamada, Y., Aikawa, K., Yamada, A. & Tateyama, Y. Sacrificial anion reduction mechanism for electrochemical stability improvement in highly concentrated Li-salt electrolyte. *J. Phys. Chem. C.* **118**, 14091–14097 (2014).

35. Pan, S.-Y. et al. Formulating a new electrolyte: synergy between low-polar and non-polar solvents in tailoring the solid electrolyte interface for the silicon anode. *ACS Appl. Mater. Interfaces* **13**, 55700–55711 (2021).

36. Petibon, R., Aiken, C. P., Ma, L., Xiong, D. & Dahn, J. R. The use of ethyl acetate as a sole solvent in highly concentrated electrolyte for Li-ion batteries. *Electrochim. Acta* **154**, 287–293 (2015).

37. Xiao, D. et al. Establishing the preferential adsorption of anion-dominated solvation structures in the electrolytes for high-energy-density lithium metal batteries. *Adv. Funct. Mater.* **31**, 2011109 (2021).

38. Zhang, S. S. & Jow, T. R. Aluminum corrosion in electrolyte of Li-ion battery. *J. Power Sources* **109**, 458–464 (2002).

39. Yamada, Y. et al. Corrosion prevention mechanism of aluminum metal in superconcentrated electrolytes. *ChemElectroChem* **2**, 1687–1694 (2015).

40. Seo, D. M., Borodin, O., Han, S.-D., Boyle, P. D. & Henderson, W. A. Electrolyte solvation and ionic association II. Acetonitrile-lithium salt mixtures: highly dissociated salts. *J. Electrochem. Soc.* **159**, A1489–A1500 (2012).

41. Gagne, R. R., Koval, C. A. & Lisensky, G. C. Ferrocene as an internal standard for electrochemical measurements. *Inorg. Chem.* **19**, 2854–2855 (1980).

42. Gritzner, G. & Kůta, J. Recommendations on reporting electrode potentials in nonaqueous solvents. *Electrochim. Acta* **29**, 869–873 (1984).

43. Wang, A., Kadam, S., Li, H., Shi, S. & Qi, Y. Review on modeling of the anode solid electrolyte interphase (SEI) for lithium-ion batteries. *NPJ Comput. Mater.* **4**, 15 (2018).

44. Yang, H. S. et al. Performance enhancement of silicon alloy-based anodes using thermally treated poly(amide imide) as a polymer binder for high performance lithium-ion batteries. *Langmuir* **32**, 3300–3307 (2016).

45. Pieczonka, N. P. W. et al. Lithium polyacrylate (LiPAA) as an advanced binder and a passivating agent for high-voltage Li-ion batteries. *Adv. Energy Mater.* **5**, 1501008 (2015).

46. Ko, S., Yamada, Y. & Yamada, A. A 4.8 V reversible Li$_2$CoPO$_4$F/graphite battery enabled by concentrated electrolytes and optimized cell design. *Batteries & Supercaps* **3**, 910 (2020).

47. Xiao, J. et al. Understanding and applying coulombic efficiency in lithium metal batteries. *Nat. Energy* **5**, 561–568 (2020).

48. Wang, J., Wolf, R. M., Caldwell, J. W., Kollman, P. A. & Case, D. A. Development and testing of a general Amber force field. *J. Comput. Chem.* **25**, 1157–1174 (2004).

49. Ryckaert, J.-P., Ciccotti, G. & Berendsen, H. J. C. Numerical integration of the cartesian equations of motion of a system with constraints: molecular dynamics of *n*-alkanes. *J. Comput. Phys.* **23**, 327–341 (1977).

50. Ryou, M. H. et al. Mussel-inspired adhesive binders for high-performance silicon nanoparticle anodes in lithium-ion batteries. *Adv. Mater.* **25**, 1571–1576 (2013).

51. He, Y. et al. Progressive growth of the solid–electrolyte interphase towards the Si anode interior causes capacity fading. *Nat. Nanotechnol.* **16**, 1113–1120 (2021).

52. He, D. et al. Collaborative design of hollow nanocubes, in situ cross-linked binder, and amorphous Void@SiO$_x$@C as a three-pronged strategy for ultrastable lithium storage. *Small* **16**, e1905736 (2020).

53. Kim, H. J. et al. Controlled prelithiation of silicon monoxide for high performance lithium-ion rechargeable full cells. *Nano Lett.* **16**, 282–288 (2016).

54. Fang, S. et al. Highly graphitized carbon coating on SiO with a π–π stacking precursor polymer for high performance lithium-ion batteries. *Polymers* **8**, 610 (2018).

55. Meng, Q. et al. High-performance lithiated SiO$_x$ anode obtained by a controllable and efficient prelithiation strategy. *ACS Appl. Mater. Interfaces* **11**, 32062–32068 (2019).

56. Wu, H. et al. Recycling silicon-based industrial waste as sustainable sources of Si/SiO$_2$ composites for high-performance Li-ion battery anodes. *J. Power Sources* **449**, 227513 (2020).

57. Huang, Q. et al. Supremely elastic gel polymer electrolyte enables a reliable electrode structure for silicon-based anodes. *Nat. Commun.* **10**, 5586 (2019).

58. Liu, Z. et al. Monodisperse and homogeneous SiO$_x$/C microspheres: a promising high-capacity and durable anode material for lithium-ion batteries. *Energy Storage Mater.* **13**, 112–118 (2018).

59. Zhao, H. et al. Toward practical application of functional conductive polymer binder for a high-energy lithium-ion battery design. *Nano Lett.* **14**, 6704–6710 (2014).

60. Liang, J. et al. A deep reduction and partial oxidation strategy for fabrication of mesoporous Si anode for lithium ion batteries. *ACS Nano* **10**, 2295–2304 (2016).

61. Zhang, Y. et al. Mechanical constraining double-shell protected Si-based anode material for lithium-ion batteries with long-term cycling stability. *J. Alloys Compd.* **846**, 156437 (2020).

62. Yan, M. Y. et al. Enabling SiO_x/C anode with high initial coulombic efficiency through a chemical pre-lithiation strategy for high-energy-density lithium-ion batteries. *ACS Appl. Mater. Interfaces* **12**, 27202–27209 (2020).

63. Cho, Y. et al. A pyrene-poly(acrylic acid)-polyrotaxane supramolecular binder network for high-performance silicon negative electrodes. *Adv. Mater.* **31**, e1905048 (2019).

64. Liu, D., Jiang, Z., Zhang, W., Ma, J. & Xie, J. Micron-sized SiO_x/N-doped carbon composite spheres fabricated with biomass chitosan for high-performance lithium-ion battery anodes. *RSC Adv.* **10**, 38524–38531 (2020).

65. He, W. et al. Efficient synthesis of N-doped SiO_x/C composite based on the defect-enriched graphite flake for lithium-ion battery. *ACS Appl. Energy Mater.* **3**, 4394–4402 (2020).

66. Hu, G. et al. Surface oxidation layer-mediated conformal carbon coating on Si nanoparticles for enhanced lithium storage. *ACS Appl. Mater. Interfaces* **13**, 3991–3998 (2021).

67. Huang, B., Huang, T., Wan, L. & Yu, A. Pre-lithiating SiO anodes for lithium-ion batteries by a simple, effective, and controllable strategy using stabilized lithium metal powder. *ACS Sustain. Chem. Eng.* **9**, 648–657 (2021).

68. Huang, B., Chu, B., Huang, T. & Yu, A. Nitrogen-doped carbon-coating disproportionated SiO materials as long cycling stable anode for lithium ion batteries. *Molecules* **26**, 1536 (2021).

69. Zhang, K. et al. SiO_x embedded in N-doped carbon nanoslices: a scalable synthesis of high-performance anode material for lithium-ion batteries. *Carbon* **178**, 202–210 (2021).

70. Sun, Q., Li, J., Hao, C. & Ci, L. Focusing on the subsequent Coulombic efficiencies of SiO_x: initial high-temperature charge after over-capacity prelithiation for high-efficiency SiO_x-based full-cell battery. *ACS Appl. Mater. Interfaces* **14**, 14284–14292 (2022).

71. Kim, J. W., Seong, M. J., Park, D. W., Jeong, G. & Yim, T. Anti-corrosive and surface-stabilizing functional electrolyte containing LiFSI and $LiPO_2F_2$ for SiO_x/NCM811-based batteries. *Corros. Sci.* **198**, 110117 (2022).

Acknowledgements

Author contributions

A.Y. conceived and directed the project, and S.K. designed the electrolyte on the basis of his thermodynamic and kinetic considerations. X.H. and S.K. conducted the experiments and analysed the data, and T.S. and N.T. performed the computational simulations. S.K. and A.Y. wrote the manuscript. S.K., N.T., Y.Y. and A.Y. supervised the research and contributed to editing the manuscript.

Competing interests

The authors declare no competing interests.

Additional information

Supplementary information The online version contains supplementary material available at https://doi.org/10.1038/s41893-023-01237-y.

Correspondence and requests for materials should be addressed to Atsuo Yamada.

Peer review information *Nature Sustainability* thanks Jie Xiao and the other, anonymous, reviewer(s) for their contribution to the peer review of this work.

Reprints and permissions information is available at www.nature.com/reprints.

Publisher's note Springer Nature remains neutral with regard to jurisdictional claims in published maps and institutional affiliations.

nature portfolio

Corresponding author(s): Atsuo Yamada

Last updated by author(s): Sep 12, 2023

Reporting Summary

Nature Portfolio wishes to improve the reproducibility of the work that we publish. This form provides structure for consistency and transparency in reporting. For further information on Nature Portfolio policies, see our Editorial Policies and the Editorial Policy Checklist.

Statistics

For all statistical analyses, confirm that the following items are present in the figure legend, table legend, main text, or Methods section.

n/a	Confirmed	
☒	☐	The exact sample size (*n*) for each experimental group/condition, given as a discrete number and unit of measurement
☐	☒	A statement on whether measurements were taken from distinct samples or whether the same sample was measured repeatedly
☒	☐	The statistical test(s) used AND whether they are one- or two-sided *Only common tests should be described solely by name; describe more complex techniques in the Methods section.*
☒	☐	A description of all covariates tested
☒	☐	A description of any assumptions or corrections, such as tests of normality and adjustment for multiple comparisons
☒	☐	A full description of the statistical parameters including central tendency (e.g. means) or other basic estimates (e.g. regression coefficient) AND variation (e.g. standard deviation) or associated estimates of uncertainty (e.g. confidence intervals)
☒	☐	For null hypothesis testing, the test statistic (e.g. F, t, r) with confidence intervals, effect sizes, degrees of freedom and P value noted *Give P values as exact values whenever suitable.*
☒	☐	For Bayesian analysis, information on the choice of priors and Markov chain Monte Carlo settings
☒	☐	For hierarchical and complex designs, identification of the appropriate level for tests and full reporting of outcomes
☒	☐	Estimates of effect sizes (e.g. Cohen's *d*, Pearson's *r*), indicating how they were calculated

Our web collection on statistics for biologists contains articles on many of the points above.

Software and code

Policy information about availability of computer code

Data collection	We have provided a full code availability statement in the manuscript
Data analysis	We have provided a full code availability statement in the manuscript

For manuscripts utilizing custom algorithms or software that are central to the research but not yet described in published literature, software must be made available to editors and reviewers. We strongly encourage code deposition in a community repository (e.g. GitHub). See the Nature Portfolio guidelines for submitting code & software for further information.

Data

Policy information about availability of data

All manuscripts must include a data availability statement. This statement should provide the following information, where applicable:
- Accession codes, unique identifiers, or web links for publicly available datasets
- A description of any restrictions on data availability
- For clinical datasets or third party data, please ensure that the statement adheres to our policy

All the relevant data are included in the paper and its Supplementary Information.

Research involving human participants, their data, or biological material

Policy information about studies with <u>human participants or human data</u>. See also policy information about <u>sex, gender (identity/presentation), and sexual orientation</u> and <u>race, ethnicity and racism</u>.

Reporting on sex and gender	N/A
Reporting on race, ethnicity, or other socially relevant groupings	N/A
Population characteristics	N/A
Recruitment	N/A
Ethics oversight	N/A

Note that full information on the approval of the study protocol must also be provided in the manuscript.

Field-specific reporting

Please select the one below that is the best fit for your research. If you are not sure, read the appropriate sections before making your selection.

☐ Life sciences   ☐ Behavioural & social sciences   ☒ Ecological, evolutionary & environmental sciences

For a reference copy of the document with all sections, see <u>nature.com/documents/nr-reporting-summary-flat.pdf</u>

Ecological, evolutionary & environmental sciences study design

All studies must disclose on these points even when the disclosure is negative.

Study description	Designing an electrolyte for the realization of a highly sustainable high-energy-density battery, in combination with a cobalt-free cathode and an earth-abundant silicon suboxide anode.
Research sample	Electrolyte solution structure, thermodynamic and kinetic factors related to the battery performance, and battery cycling data
Sampling strategy	N/A
Data collection	The detail is described in the methods section in the main text.
Timing and spatial scale	N/A
Data exclusions	N/A
Reproducibility	The reproducibility of battery performance with a new electrolyte has been confirmed. All the data is summarized in Supplementary Table 4.
Randomization	N/A
Blinding	N/A

Did the study involve field work?   ☐ Yes   ☒ No

Reporting for specific materials, systems and methods

We require information from authors about some types of materials, experimental systems and methods used in many studies. Here, indicate whether each material, system or method listed is relevant to your study. If you are not sure if a list item applies to your research, read the appropriate section before selecting a response.

Materials & experimental systems

n/a	Involved in the study
☒	Antibodies
☒	Eukaryotic cell lines
☒	Palaeontology and archaeology
☒	Animals and other organisms
☒	Clinical data
☒	Dual use research of concern
☒	Plants

Methods

n/a	Involved in the study
☒	ChIP-seq
☒	Flow cytometry
☒	MRI-based neuroimaging